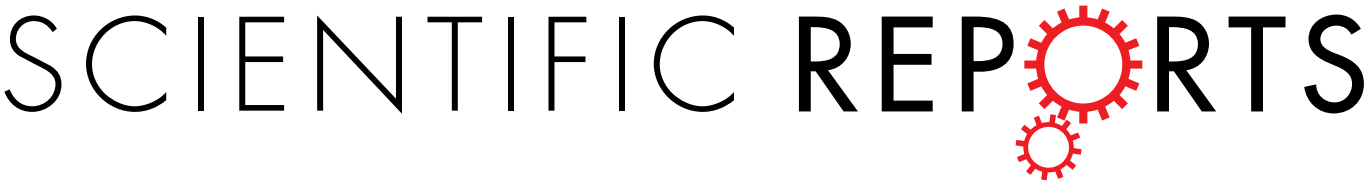

OPEN

The Effect of Preparation Conditions on Raman and Photoluminescence of Monolayer WS_2

Received: 15 June 2016
Accepted: 15 September 2016
Published: 18 October 2016

Kathleen M. McCreary[1], Aubrey T. Hanbicki[1], Simranjeet Singh[2], Roland K. Kawakami[2], Glenn G. Jernigan[1], Masa Ishigami[3], Amy Ng[1], Todd H. Brintlinger[1], Rhonda M. Stroud[1] & Berend T. Jonker[1]

We report on preparation dependent properties observed in monolayer WS_2 samples synthesized via chemical vapor deposition (CVD) on a variety of common substrates (Si/SiO_2, sapphire, fused silica) as well as samples that were transferred from the growth substrate onto a new substrate. The as-grown CVD materials (as-WS_2) exhibit distinctly different optical properties than transferred WS_2 (x-WS_2). In the case of CVD growth on Si/SiO_2, following transfer to fresh Si/SiO_2 there is a ~50 meV shift of the ground state exciton to higher emission energy in both photoluminescence emission and optical reflection. This shift is indicative of a reduction in tensile strain by ~0.25%. Additionally, the excitonic state in x-WS_2 is easily modulated between neutral and charged exciton by exposure to moderate laser power, while such optical control is absent in as-WS_2 for all growth substrates investigated. Finally, we observe dramatically different laser power-dependent behavior for as-grown and transferred WS_2. These results demonstrate a strong sensitivity to sample preparation that is important for both a fundamental understanding of these novel materials as well as reliable reproduction of device properties.

The novel properties of graphene have stimulated research in other two-dimensional (2D) materials such as hexagonal boron nitride and the transition metal dichalcogenides (TMDs). The TMDs have a chemical composition of MX_2 (where M = Mo, W and X = S, Se), and monolayer building blocks of these materials are composed of three sheets of atoms where a top and bottom chalcogen layer encapsulate the center metal sheet. While much of the early work focused on monolayer MoS_2, the closely related WS_2 exhibits superior optical properties[1–3] and larger spin-orbit coupling[4], motivating further extensive investigation. WS_2 exhibits a strong sensitivity to layer number, with the band structure transitioning from an indirect-gap semiconductor for bulk WS_2 to direct-gap semiconductor at monolayer thickness[1]. Fundamental investigations and prototype devices incorporating atomically thin WS_2 have demonstrated reasonable electronic mobility[5,6], high optical responsivity[1], robust device performance following repeated bending[7], high valley polarization[8–10], and long spin lifetimes[11,12]. These properties make WS_2 a promising material for a variety of applications including photodetection, flexible electronics, and spintronics.

Monolayers of TMDs can be obtained using a variety of methods including mechanical and chemical exfoliation, atomic layer deposition (ALD)[13], molecular beam epitaxy (MBE)[14], and chemical vapor deposition (CVD)[15]. Other innovative options continue to be explored. The CVD approach has emerged as a particularly reliable route to obtain uniform, high-quality, large-area samples[2,16,17], with wafer-scale synthesis of WS_2 recently demonstrated[18]. Due to the elevated temperatures necessary for CVD synthesis, rigid and thermally robust substrates such as SiO_2 or Al_2O_3 are commonly used.

The ability to transfer films off the growth substrate provides a means to incorporate TMDs with a more diverse array of materials, and is highly desirable for both fundamental investigations and applications. For

[1]Naval Research Laboratory, Washington DC 20375, USA. [2]Department of Physics, The Ohio State University, Columbus OH 43210, USA. [3]Department of Physics and Nanoscience Technology Center, University of Central Florida, Orlando, FL 32816-2385, USA. Correspondence and requests for materials should be addressed to K.M.M. (email: kathleen.mccreary@nrl.navy.mil)

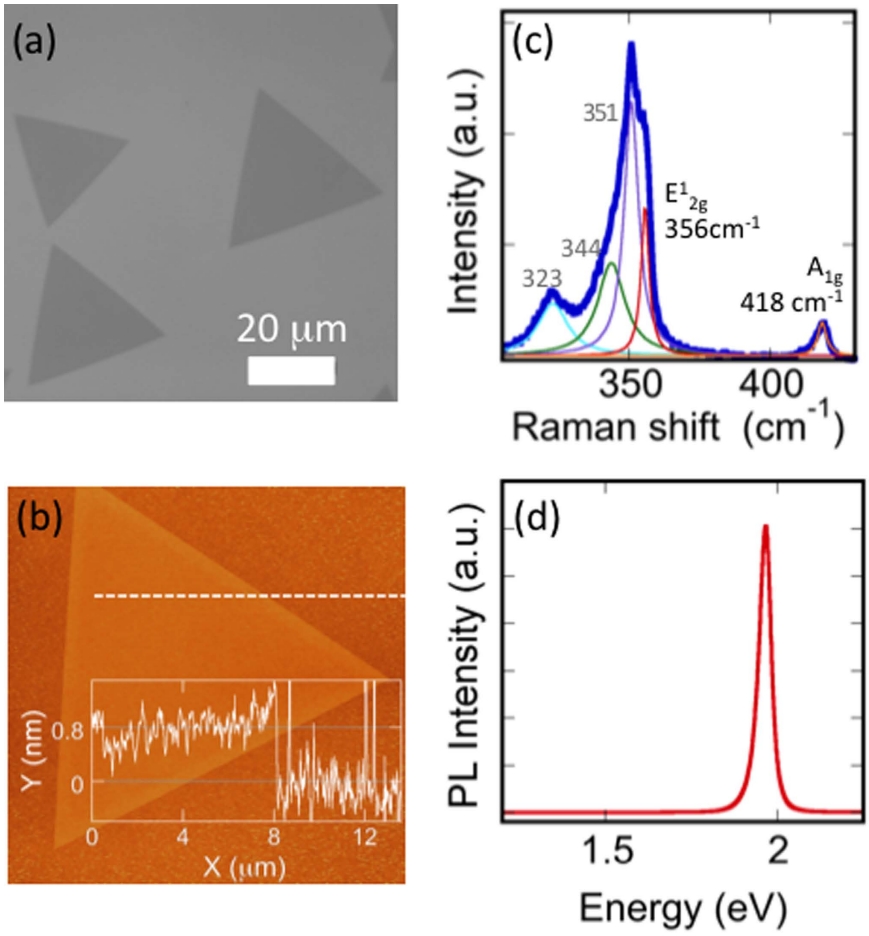

Figure 1. Characterization of monolayer WS_2 synthesized on Si/SiO_2. (**a**) Optical microscope images display randomly oriented equilateral triangular growth. (**b**) The AFM image is obtained on a representative WS_2 triangle. A height profile (inset) is measured along the dashed line and shows a step height of ~0.8 nm. (**c**) Raman spectroscopy and (**d**) photoluminescence measurements confirm monolayer WS_2.

instance, transfer to high-k dielectrics may provide a means to modify excitonic properties such as binding energies, position, and radii, as Coulomb interactions are sensitive to the local environment[19,20]. The construction of van der Waals heterostructures (vdwh) through sequential stacking of 2D materials is also expected to open the door to new device functionality, and is a rapidly progressing area of research[21] with recent reports of interlayer excitons[22], ultrafast charge separation[23], and long valley lifetimes[24] in TMD based vdwh. While reliable transfer techniques will certainly be important as the field continues to grow, there are limited reports that investigate if and how WS_2 is impacted[25–27]. Additionally, such studies typically transfer between dissimilar materials (i.e. sapphire to Si/SiO_2), making it difficult to determine the source of any observed modifications. Therefore, it is important to first understand and evaluate any changes brought about by transfer processes between identical substrates so that future investigations may accurately isolate, identify and assess modifications resulting from interactions with various materials. In this letter we directly compare fundamental properties of CVD synthesized monolayer WS_2 between the as-grown state (as-WS_2) and after removal from the growth substrate and transfer to a fresh supporting substrate (x-WS_2).

Results and Discussion

Monolayer tungsten disulfide is synthesized at a growth temperature of 825 °C in a 2-inch diameter quartz tube furnace. Powdered WO_3 (Alfa Aesar 13398) and sulfur (Alfa Aesar 10755) serve as precursors for the synthesis. Additional details can be found in reference[16]. Typically Si/SiO_2 (275 nm) is employed as growth substrate and is the main focus of this manuscript. However, monolayer WS_2 has also been realized on c-plane sapphire and fused silica substrates, and will be briefly discussed. Growth on Si/SiO_2 results in multiple triangular islands exhibiting lateral dimensions ranging from a few to several tens of microns, as shown in the optical image, Fig. 1(a). The equilateral triangle morphology is characteristic of single-crystal growth[28]. Examination of a WS_2 triangle using AFM (Fig. 1(b)) shows uniform thickness across the triangle as well as a step height of ~0.8 nm (inset of Fig. 1(b)), consistent with monolayer WS_2.

Raman and photoluminescence (PL) spectroscopy measurements are performed using a commercial Horiba LabRam confocal spectrometer in ambient atmosphere at room temperature using 532 nm laser excitation unless otherwise stated. A 100× objective focuses the laser beam to a spot with ~1 μm diameter. Raman spectroscopy is

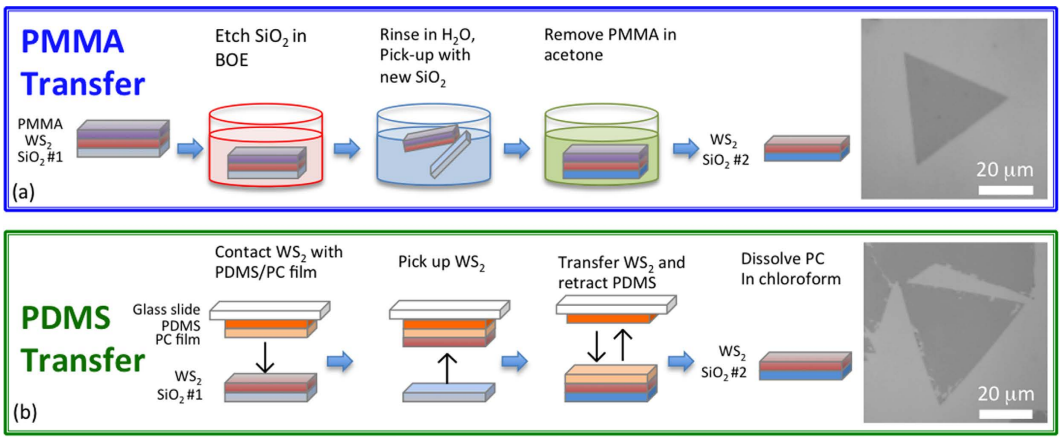

Figure 2. Schematic of the two transfer methods. (**a**) For PMMA transfer, the sample is coated with a thin layer of PMMA then submerged in BOE to remove the SiO_2. Once fully etched, the film is rinsed in H_2O then picked up with the target substrate. An acetone soak removes the PMMA. An optical image of PMMA transferred WS_2 exhibits a uniform, clean, triangular shape. (**b**) For the PDMS transfer, a PDMS/PC film is carefully brought into contact with the desired WS_2 then retracted. This moves the WS_2 from Si/SiO_2 onto the PDMS/PC film. The PDMS/PC/WS_2 stack is then placed onto clean Si/SiO_2. The PDMS stamp is retracted, leaving the PC film on the top surface of WS_2, which is then dissolved in chloroform. An optical image following PDMS transfer is shown on the right.

a quick and reliable method for layer identification in WS_2[29,30]. In addition to the in-plane (E^1_{2g}) and out-of-plane (A^1_g) first order optical modes, 532 nm laser excitation results in second-order resonant peaks involving longitudinal acoustic modes (LA(M)). A typical Raman spectrum from as-WS_2 is show in Fig. 1(c). A multi-lorentzian fit clearly resolves the individual components, with E^1_{2g} and A^1_g peaks located at 355.7 cm^{-1} and 418.4 cm^{-1}, respectively. A PL spectrum (Fig. 1(d)), also measured on as-WS_2, shows a single peak having maximum intensity at ~1.96 eV, confirming the single layer nature. While sample-to-sample variation can influence the exact PL peak position, repeated measurements obtained across multiple samples as well as separate monolayer regions on the same sample typically exhibit peak emission intensity within ~10 meV of 1.96 eV for monolayer WS_2 synthesized on Si/SiO_2 (275 nm).

Two distinct methods are used to remove WS_2 monolayers from their growth substrates and transfer them to a fresh Si/SiO_2 substrate. The first method is referred to as "PMMA transfer" and involves a wet etching process based on previous techniques used for transferring CVD graphene grown on copper[31]. This process is illustrated in Fig. 2(a) and is described in the Methods. Optical images of PMMA x-WS_2 (Fig. 2(a), right panel) demonstrate the shape and uniformity of the flakes are maintained after transfer. Additionally, transmission electron microscope images of PMMA x-WS_2 (Supplementary information) display a uniform, defect-free lattice composed of W and S atoms, indicating the high quality monolayer WS_2 is preserved throughout the process. The second transfer method is free of wet etchants and ensures a clean substrate-sample interface. This method, termed "PDMS stamp", is illustrated in Fig. 2(b) and is also described in the Methods. This technique provides microscopic precision for both placement and rotation angle of the transferred WS_2. The optical image in Fig. 2(b) (right panel) displays a typical PDMS transferred region. The majority of the sample exhibits uniform contrast, although at the edges there are small patches where WS_2 is absent.

PL, reflectivity and Raman spectra obtained from representative as-WS_2 and PMMA x-WS_2 are presented in Fig. 3. The spectrum for as-WS_2 (Fig. 3(a)) exhibits a peak PL emission at 1.956 eV, with a FWHM of 35 meV. A considerable blue shift of ~50 meV is evident in the x-WS_2 spectrum, where the emission peak shifts to 2.011 eV and the FWHM is reduced to 27 meV. Control samples were fabricated by coating as-WS_2 with PMMA then removing it. These samples show no shift in peak position, ruling out doping from PMMA residue as the source of the PL shift.

In conjunction with PL measurements, reflectivity measurements are obtained from the same spot on the sample. Light from a white light source is focused though a 50× objective onto the sample and reflected intensity is measured. To minimize unwanted contributions from the substrate, the difference between the intensity measured from the bare substrate (I_{off}), and from the WS_2 sample (I_{on}) is obtained then normalized to the substrate intensity, $I^* = (I_{off}-I_{on})/I_{off}$. The peak reflectivity measured at 1.961 eV (2.015 eV) for as-WS_2 (PMMA x-WS_2) is nearly coincident with PL measurements, although there is a small difference in peak energy. This measured Stokes shift provides information regarding the doping level of TMDs, as Stokes shifts are known to increase monotonically with the doping level[32]. The small, $\leq$5 meV Stokes shift observed in both the as-grown and transferred samples is comparable to or less than that observed in exfoliated WS_2 monolayers[1,8], and indicates that a low doping level is achieved in as-grown material and maintained throughout the transfer process.

Raman spectra also show considerable change after PMMA transfer (Fig. 3 (c–h)). Measurements are performed with excitation energies of both 532 nm and 488 nm in an effort to reduce the resonant 2LA contribution. For both laser excitations, the relative intensities of the dominant E^1_{2g}, A_{1g}, and 2LA modes show considerable differences before and after transfer. We surmise that the transfer process increases the WS_2-to-substrate distance,

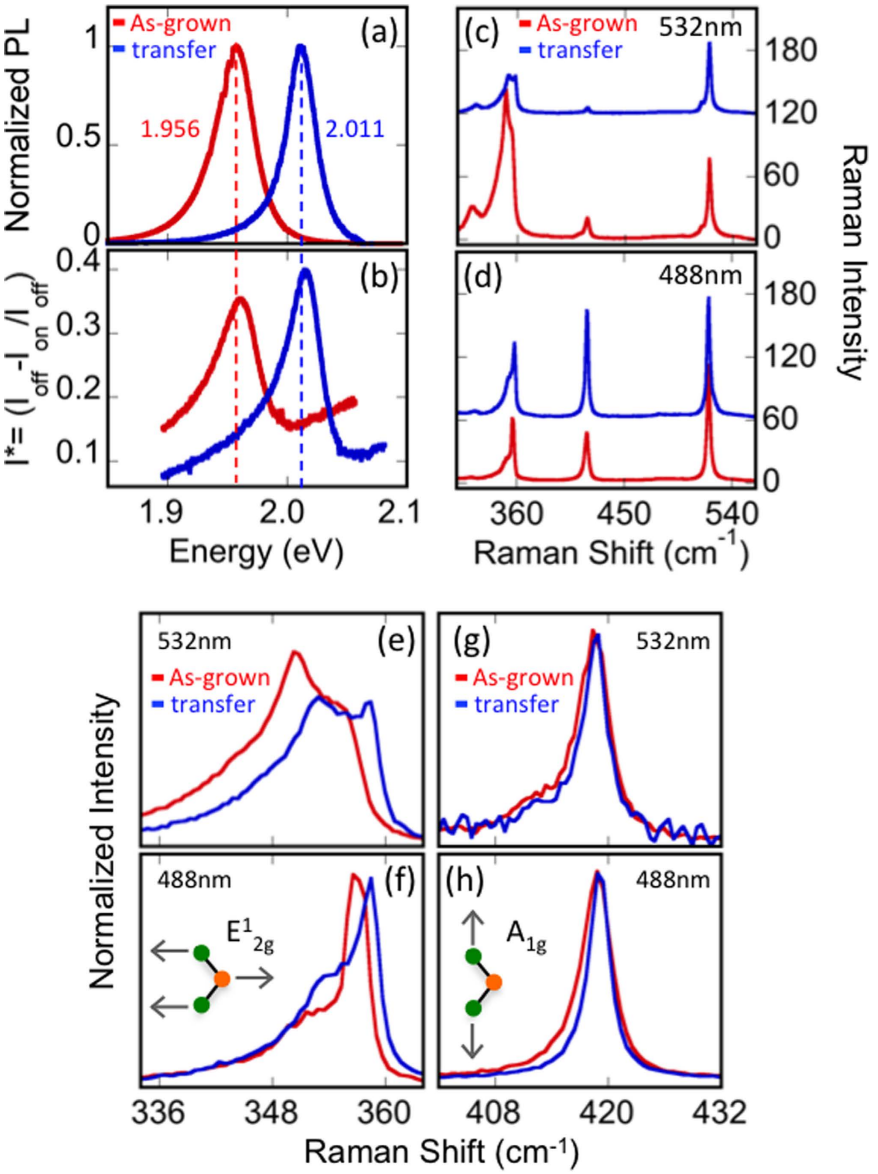

Figure 3. PL, reflectivity, and Raman characterization before and after PMMA transfer. (**a**) PL emission and (**b**) reflectivity shift to higher energy following transfer. A $\leq$ 5 meV difference in PL and reflectivity spectra is measured for both as-grown and transferred WS_2. The vertical red and blue dashed lines indicate the peak PL position and highlight the small Stokes shift. Raman spectra are measured using (**c**) 532 nm and (**d**) 488 nm excitation. As-grown and transferred spectra are offset for clarity. The relative intensities of E^1_{2g}, A_{1g}, and 2LA vary before and after. The intensity of the Si substrate peak (520.7 cm^{-1}) is unaffected. (**e,f**) The transfer process shifts the in-plane Raman mode to higher wavenumber while out-of-plane (**g,h**) remains constant. Schematic diagrams of the E^1_{2g} and A_{1g} Raman modes are displayed in the inset of (**f,h**), respectively. The changes in optical properties indicate the transfer process removes tensile strain.

leading to differences in optical interference, which in turn affects the Raman peak intensity[33,34]. These complicated interference effects are sensitive to both laser excitation energy as well as the energy of the Raman emission, and can thereby enhance one Raman peak while reducing the intensity of a second, as seen in Fig. 3(c,d). Therefore, it is instructive to carefully examine any alterations in peak positions (Fig. 3(e–h)).

The position of the out-of-plane A_{1g} mode in TMD monolayers is sensitive to doping level, and red-shifting occurs with increasing electron concentration, while E^1_{2g} is unaffected by doping levels[3,35]. Conversely only the E^1_{2g} mode is impacted by strain, and exhibits a red-shift as a result of uniaxial and biaxial strain[36,37]. For both the 532 nm and 488 nm laser excitations there is a clear ~1 cm^{-1} shift in the E^1_{2g} peak (Fig. 3(e,f)), whereas the A_{1g} peak position is unchanged (Fig. 3(g,h)). X-ray photoelectron spectroscopy comparing as-WS_2 and x-WS_2 excludes changes in chemical composition as the source of the observed differences in Raman spectra (Supplementary information). Instead, the observed shift is consistent with a reduction of tensile strain[38,39]. The tensile strain arises due to the differences in the thermal expansion coefficient of the monolayer WS_2 and the

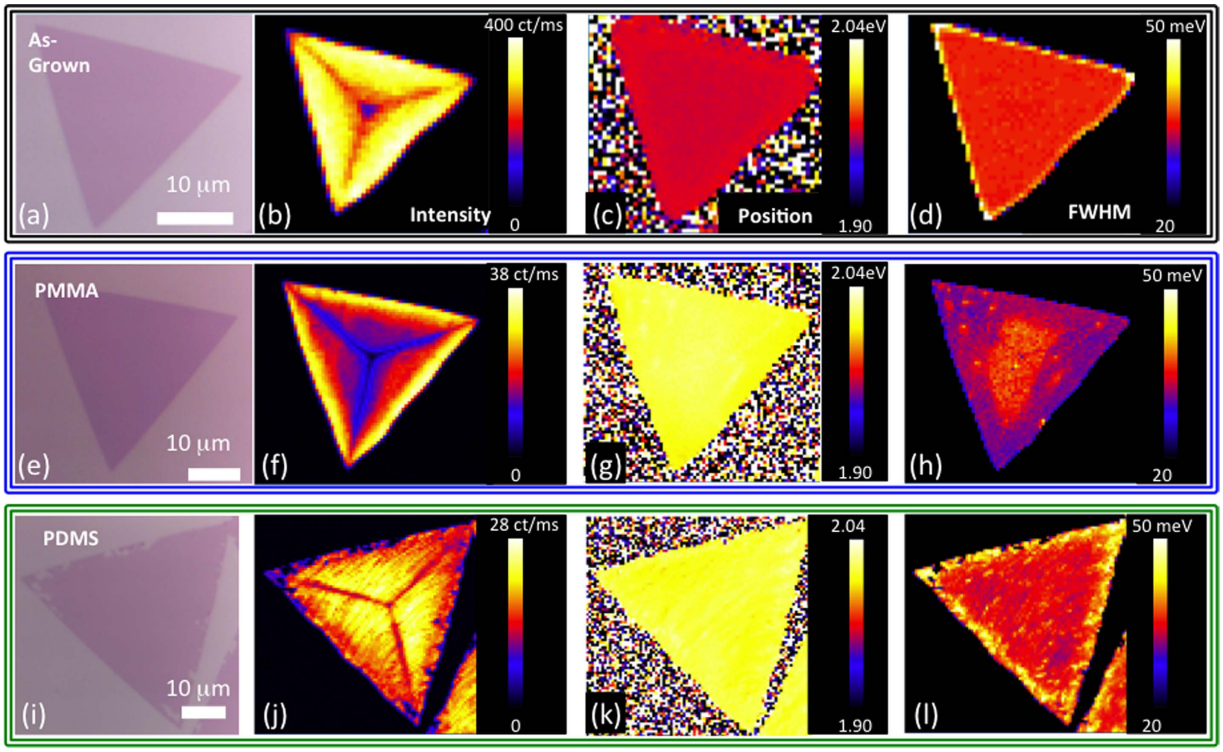

Figure 4. Optical images and PL maps comparing as-grown and transferred WS_2. (**a**) Optical microscopy of as-grown WS_2 and corresponding maps of (**b**) PL intensity, (**c**) PL emission position, and (**d**) FWHM. (**e**) Optical microscopy of PMMA transferred WS_2 and corresponding maps of (**f**) PL intensity, (**g**) PL emission position, and (**h**) FWHM. (**i**) Optical microscopy of PDMS transferred WS_2 and corresponding maps of (**j**) PL intensity, (**k**) PL emission position, and (**l**) FWHM. Similar patterns in PL intensity are observed for all three samples, with low intensity at the center of the triangle and directed outward toward the three corners. PMMA and PDMS transferred samples have noticeably higher emission energy, resulting from the removal of strain.

supporting substrate. As the substrate and WS_2 cool to room temperature from growth temperature (e.g. 825° C), the two contract at different rates, imparting strain to the WS_2 monolayer. The transfer process subsequently removes the strain. The presence of tensile strain is expected to reduce the band gap of WS_2 at a rate of 0.2 eV per % strain[26,38]. We therefore estimate the strain present in as-WS_2 on Si/SiO_2 to be ~0.25% based on the ~50 meV shift in PL emission measured before and after transfer.

Sample uniformity is investigated across representative ~30 μm triangles. Detailed maps (Fig. 4) show the PL intensity, peak position, and FWHM for as-grown WS_2 on Si/SiO_2 compared to WS_2 synthesized on Si/SiO_2 and subsequently transferred to fresh Si/SiO_2 using both PMMA and PDMS transfer methods. The PL emission from as-WS_2 (Fig. 4(b–d)) exhibits considerable variation across the sample. The perimeter exhibits high PL intensity, with low intensity regions in the center that extend radially outward toward the three corners, similar to previous reports[17,28]. Despite the variation in PL intensity, the peak position and FWHM (Fig. 4c,d) are highly uniform across the sample, with average values of 1.964 eV and 36 meV, respectively.

The PMMA x-WS_2 (Fig. 4(f–h)) exhibits a similar spatial pattern in PL intensity, with low intensity at the center and high intensity along the edges. Overall, the PL emission undergoes a blueshift of ~50 meV, exhibiting an average value of 2.012 eV, while the average FWHM is 32 meV. The similarity in PL intensity patterns for as-grown and transferred samples combined with the uniformity in peak position and FWHM exclude local variations in strain or doping as the cause of the non-uniform PL intensity[40], but instead points to structural defects as the source of non-uniformity. The PL intensity of PDMS x-WS_2 (Fig. 4(j–l)) is comparable to the PMMA transfer, with qualitatively similar PL intensity variations across the triangle, and uniform emission energy at 2.013 eV and average FWHM of 36 meV. The edges exhibit a slightly higher FWHM relative to the interior, most likely due to the tears, which are evident in the optical images. While some sample-to-sample variation is observed in emission energy following transfer, the overall shift to higher emission energy is highly repeatable, typically resulting in emission above 2.0 eV.

An investigation of the relationship between emission spectra and laser excitation power is presented in Fig. 5. Recent reports have shown that exposure to a high intensity laser can enhance trionic[8,41] emission as well as induce biexciton[42,43] emission in WS_2. As is evident from the normalized PL spectra of as-WS_2 emission (Fig. 5(a)), there is a single peak for all incident powers spanning over four orders of magnitude, consistent with emission from the neutral exciton (X^0). The integrated PL intensity is obtained within the range from 1.65 eV to 2.2 eV at each laser power (Fig. 5(d)) and is well described by a linear relationship (black line). The linearity is indicative of emission from the neutral exciton with an absence of exciton-exciton recombination. Additionally,

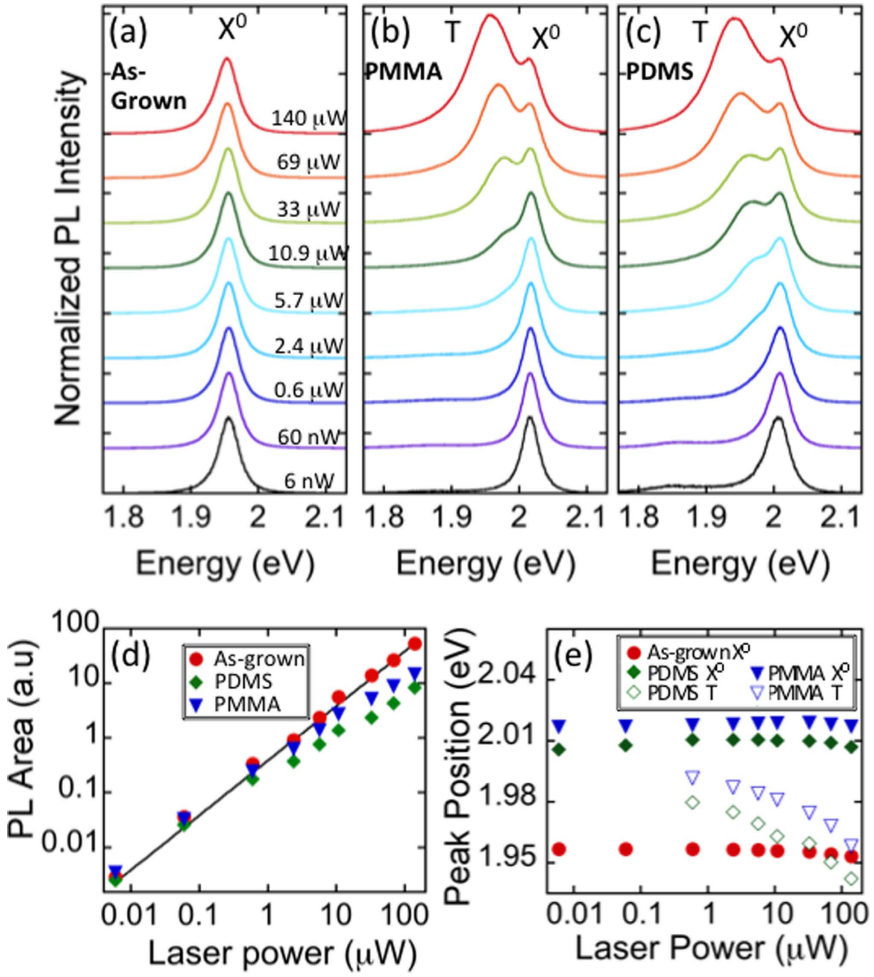

Figure 5. Laser power dependence in ambient conditions. (**a**) For as-grown WS_2, the spectral shape of PL is unaffected by increased laser power, with emission occurring from the neutral exciton, X^0, for all excitation conditions. In (**b**) PDMS and (**c**) PMMA transferred samples, X^0 emission dominates at low powers, but the trion, T, dominates at high power excitation. (**d**) PL integrated area from 1.65 to 2.2 eV and (**e**) peak positions for the three samples.

the PL peak position of the as-WS_2 is nearly constant, showing only a slight decrease at the highest laser powers investigated, (Fig. 5(e)) likely due to heating effects.

Transferred samples exhibit considerably different behavior under identical excitation conditions. At low power, both PMMA (Fig. 5(b)) and PDMS (Fig. 5(c)) x-WS_2 are in the neutral excitonic state, X^0. As laser power steadily increases, a low energy shoulder emerges then quickly develops into the dominant emission peak. The lower emission energy and larger FWHM identify the second emission peak as the charged exciton, or trion (T)[41]. The integrated PL intensity of transferred samples begins to deviate from the linear relationship above 1 μW laser power, exhibiting lower integrated area as laser power increases (Fig. 5(d)). The decrease in emission is consistent with a transfer from X^0 to T dominated emission, as emission from charged trions is known to be lower in intensity due to increased non-radiative recombination mechanisms such as Auger recombination or exciton-exciton annihilation[3,8,44]. The position of the neutral exciton is nearly stable throughout the range of laser powers, undergoing a small redshift (<5 meV) only at the highest powers. Such behavior is similar to that observed in as-WS_2 and suggests the heat transferred to the substrate is comparable for both as-WS_2 and x-WS_2. The trion in x-WS_2, however, exhibits a clear redshift with increasing laser power (Fig. 5(e)), resulting in an increasing separation between X^0 and T. The separation between neutral and charged excitons is linearly dependent on the Fermi level and is described by,

$$E_{X0} - E_T = E_{b,T} + E_F$$

where E_{X0} is the energy position of the neutral exciton, E_T is the position of the trion, $E_{b,T}$ is the trion binding energy, and E_F is the Fermi level[32,42]. The PMMA (PDMS) transferred sample exhibits a separation of 26 meV (30 meV) at the 1 μW excitation, providing an upper bound for the trion binding energy, consistent with previous results on mechanically exfoliated WS_2[42,44].

Tunability between X^0 and T emission has previously been demonstrated in mechanically exfoliated monolayer TMDs following high powered laser exposure or annealing procedures. The likely source of the tunability is the removal or adsorption of p-type oxygen containing adsorbates[41,45–49]. We note that all our samples are measured in an ambient environment and are therefore exposed to similar concentrations of adsorbates. The stark contrast we observe between as-grown and transferred WS_2 thus suggests very different adsorption/desorption mechanisms are present on the two types of samples. In studies of the related 2D material graphene, it has been shown that surface deformations impact sample-adsorbate interactions. Specifically, binding at local sites becomes more energetically favorable[50]. Microscopic profile fluctuations are common in mechanically exfoliated or transferred materials due to transfer-induced wrinkles or trapped chemicals[51–53]. This effect may be significantly reduced for as-grown materials on a rigid substrate, explaining the lack of tunability on these types of samples. Additionally, differences in sample-substrate interactions are also expected to impact adsorption behaviors. Some mechanisms include variations in strain[54–56], out-of-plane relaxation at binding sites[57,58], and accessibility to top and bottom surfaces[56].

Synthesis of WS_2 on substrates with different thermal expansion coefficients (α) provides a means to independently modify the strain in WS_2 via the growth cooldown and subsequently monitor the sensitivity to laser power. Using the same procedure as reported above, we synthesize monolayer WS_2 on fused silica and c-plane sapphire. The coefficients of thermal expansion for silica and sapphire are 0.55 and 9.7×10^{-6}/K, respectively. The thermal expansion coefficient for WS_2 is expected to be in the range $7 < \alpha < 10 \times 10^{-6}$/K based on theoretical investigations[59] and experimentally measured bulk values[60]. As with the growth of WS_2 on Si/SiO_2, triangular growth is evident on both fused silica and sapphire substrates (Fig. 6). Maps of the PL peak positions are presented in Fig. 6(a,b). WS_2 synthesized on fused silica exhibits uniform emission energy across the triangle, with an average PL peak position of 1.94 eV. In contrast, WS_2 on sapphire results in the considerably higher average emission energy of 1.99 eV, and a large variation in peak position (1.95–2.02 eV). This large variation on sapphire could arise from factors such as substrate impurities or water intercalation[25] and is under investigation.

The energy position of PL emission and associated Raman spectra (Supplementary information) demonstrate that synthesis on the low-α fused silica substrates induce considerable strain in WS_2 whereas growth on sapphire approaches a strain-free system. Power-dependent PL spectra are shown in Fig. 6 (c,d) for as-grown samples on both fused silica and sapphire. Based on a value of 2.105 eV for an unstrained WS_2 monolayer, the WS_2 on fused silica (sapphire) exhibits ~0.39% (0.08%) strain. In both cases, the spectral shape and position are unaffected by laser power. Additionally, the integrated area of the PL emission follows a linear behavior for all laser powers used, indicating the excitonic behavior is not modified with increasing laser power. Therefore, while as-grown WS_2 on Si/SiO_2, sapphire, and fused silica exhibit distinctly different strain amounts, optical control of the excitonic state is absent, suggesting strain has minimal impact on adsorption and desorption mechanisms of O_2 containing species.

Conclusion

In conclusion, we have demonstrated that the choice of growth substrate determines the PL emission energy of the neutral exciton, X^0. The emission energy is governed by strain in the as-grown WS_2 and arises from differences in thermal expansion coefficient between WS_2 and the supporting substrate. The strain can be removed by transferring the sample off of the growth substrate. This process results in the emission shifting to higher energy. We also observe a different response to laser power for as-grown versus transferred samples. Transferred samples exhibit extreme sensitivity to laser power, with X^0 emission dominating at low laser power, but transitioning to T emission as power is increased. As-grown materials show no variation in spectral shape or position of PL as laser power is increased by more than four orders of magnitude. We speculate that the distinctly different power-dependent behaviors result primarily from different adsorption and/or desorption mechanisms in as-grown and transferred WS_2. Differences in interfacial effects such as electron transfer between WS_2 and supporting substrates could also influence the observed behaviors. The more intimate WS_2-substrate contact present in as-WS_2 may promote more efficient electron transfer from WS_2 to the substrate, hindering trion formation. Theoretical modeling and continued experimental investigation are necessary to identify the precise source of disparity observed in as-WS_2 and x-WS_2.

The moderate laser powers used in this work are comparable to conditions typically utilized for optical characterization of TMDs. This highlights that care is required to prevent laser excitation-induced effects in transferred materials. Additionally, we speculate that investigations involving chemical sensing and defect passivation will be distinctly different for as-grown and transferred/exfoliated materials, as both are intimately related to adsorption and desorption mechanisms. Finally, we note this work is the first to report such dramatically different power-dependent behavior for as-grown and transferred WS_2. This study should therefore stimulate further experimental and theoretical investigations in the field.

Methods

Sample preparation "PMMA transfer". A thin layer of polymethyl methacrylate (PMMA) is spun onto the surface of the entire growth substrate then submerged in buffered oxide etchant. After several hours, the oxide layer is removed, freeing the WS_2/PMMA film from the growth substrate. The sample is subsequently transferred to H_2O to rinse chemical etchants, where the fresh Si/SiO_2 is used to lift the film out of the water. A 2000 rpm spin and 150 °C bake improve the uniformity and adhesion to the substrate, after which the PMMA is dissolved in acetone.

Sample preparation "PDMS transfer". A polydimethylsiloxane (PDMS) stamp coated with polycarbonate (PC) is carefully brought into contact with the desired monolayer region. The van der Waals forces

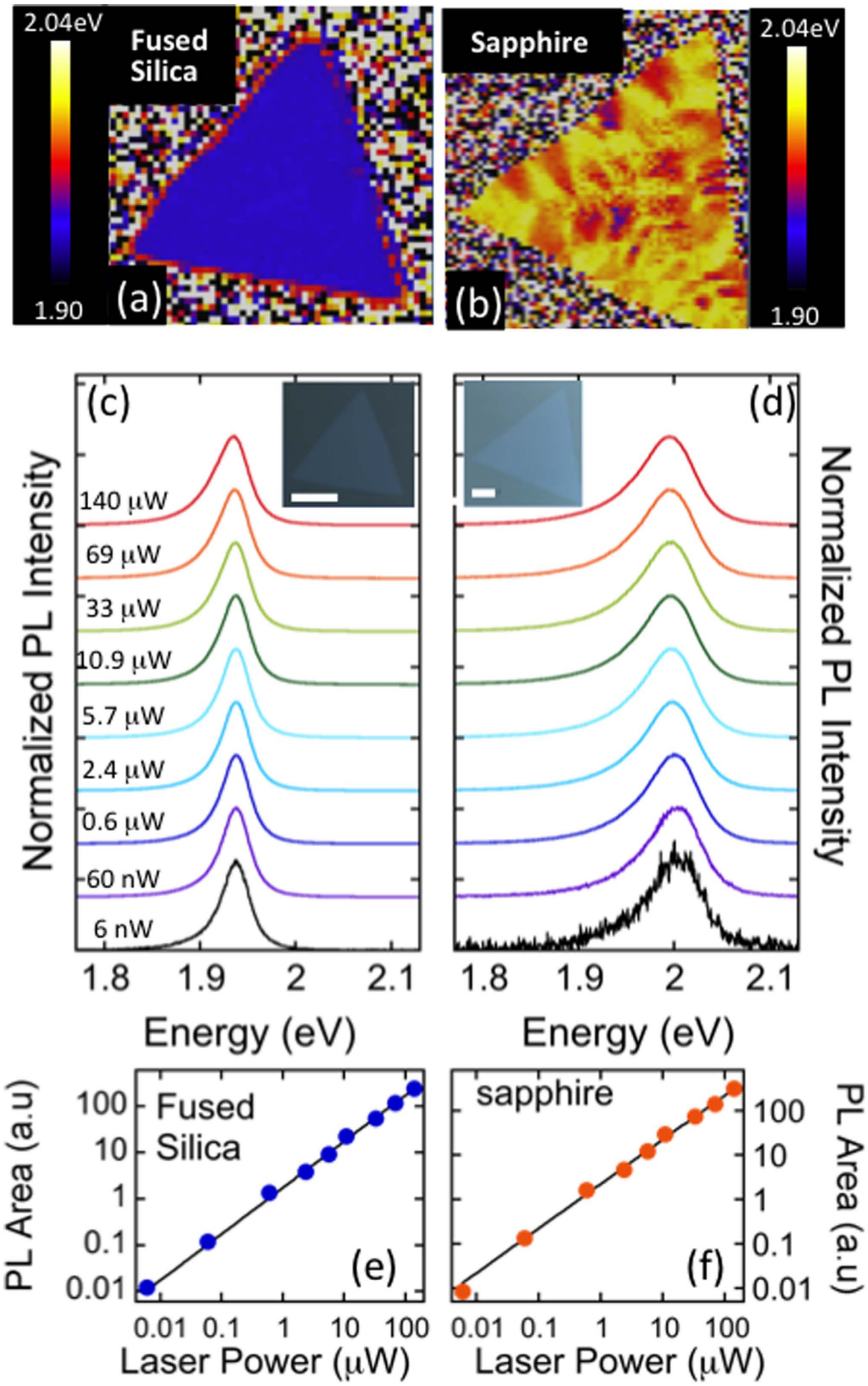

Figure 6. Characterization of monolayer WS_2 synthesized on various substrates. (**a,b**) Maps of PL position for WS_2 monolayers grown on fused silica and sapphire, respectively. The average peak position on silica (sapphire) is 1.94 ev (1.99 eV). The dissimilar thermal expansion coefficients of silica and sapphire lead to different strain in WS_2 and the differences in peak position. The position and spectral shape of PL emission is unaffected by increased laser power for both (**c**) silica and (**d**) sapphire. (**e,f**) Integrated area is linearly related to laser power for both silica and sapphire. The insets of (**c,d**) show optical images of the mapped WS_2 monolayers. The scale bar is 10 μm.

between the PC are strong enough to remove the WS_2 from the supporting substrate. Once on the stamp, the WS_2 can be positioned or rotated to a desired angle before being brought into contact and released onto the desired substrate with a gentle thermal anneal.

Transmission electron microscopy. Samples are prepared for TEM imaging using the PMMA transfer process. Following the rinse in deionized H_2O, the WS_2/PMMA film is picked up using a Quantifoil TEM grid and subsequently baked at 150 °C on a hot plate. PMMA is removed using acetone, making the grid ready for the

TEM imaging. Scanning transmission electron microscopy is performed on a Nion UltraSTEM-X 200 instrument operating at 60 kV accelerating voltage.

X-ray Photoelectron Spectroscopy. Spectra are obtained with monochromated Al Kα radiation using a 400 μm aperture.

References

1. Zhao, W. *et al.* Evolution of Electronic Structure in Atomically Thin Sheets of WS_2 and WSe_2. *ACS Nano* **7,** 791–797 (2013).
2. Gutiérrez, H. R. *et al.* Extraordinary Room-Temperature Photoluminescence in Triangular WS_2 Monolayers. *Nano Lett.* **13,** 3447–3454 (2013).
3. Peimyoo, N. *et al.* Chemically Driven Tunable Light Emission of Charged and Neutral Excitons in Monolayer WS_2. *ACS Nano* **8,** 11320–11329 (2014).
4. Zeng, H. *et al.* Optical signature of symmetry variations and spin-valley coupling in atomically thin tungsten dichalcogenides. *Sci. Rep.* **3,** 1608 (2013).
5. Iqbal, M. W. *et al.* High-mobility and air-stable single-layer WS_2 field-effect transistors sandwiched between chemical vapor deposition-grown hexagonal BN films. *Sci. Rep.* **5,** 10699 (2015).
6. Ovchinnikov, D., Allain, A., Huang, Y.-S., Dumcenco, D. & Kis, A. Electrical Transport Properties of Single-Layer WS_2. *ACS Nano* **8,** 8174–8181 (2014).
7. Gong, Y., Carozo, V., Li, H., Terrones, M. & Jackson, T. N. High flex cycle testing of CVD monolayer WS_2 TFTs on thin flexible polyimide. *2D Mater.* **3,** 021008 (2016).
8. Hanbicki, A. T. *et al.* Anomalous temperature-dependent spin-valley polarization in monolayer WS_2. *Sci. Rep.* **6,** 18885 (2016).
9. Zhu, B., Zeng, H., Dai, J., Gong, Z. & Cui, X. Anomalously robust valley polarization and valley coherence in bilayer WS_2. *Proc. Natl. Acad. Sci.* **111,** 11606–11611 (2014).
10. Nayak, P. K., Lin, F.-C., Yeh, C.-H., Huang, J.-S. & Chiu, P.-W. Robust room temperature valley polarization in monolayer and bilayer WS_2. *Nanoscale* **8,** 6035–6042 (2016).
11. Yang, L. *et al.* Long-lived nanosecond spin relaxation and spin coherence of electrons in monolayer MoS_2 and WS_2. *Nat. Phys.* **11,** 830–834 (2015).
12. Bushong, E. J. *et al.* Imaging Spin Dynamics in Monolayer WS2 by Time-Resolved Kerr Rotation Microscopy. *ArXiv160203568 Cond-Mat* (2016).
13. Song, J.-G. *et al.* Layer-Controlled, Wafer-Scale, and Conformal Synthesis of Tungsten Disulfide Nanosheets Using Atomic Layer Deposition. *ACS Nano* **7,** 11333–11340 (2013).
14. Zhang, Y. *et al.* Direct observation of the transition from indirect to direct bandgap in atomically thin epitaxial $MoSe_2$. *Nat Nano* **9,** 111–115 (2014).
15. Zhan, Y., Liu, Z., Najmaei, S., Ajayan, P. M. & Lou, J. Large-Area Vapor-Phase Growth and Characterization of MoS_2 Atomic Layers on a SiO2 Substrate. *Small* **8,** 966–971 (2012).
16. McCreary, K. M., Hanbicki, A. T., Jernigan, G. G., Culbertson, J. C. & Jonker, B. T. Synthesis of Large-Area WS_2 monolayers with Exceptional Photoluminescence. *Sci. Rep.* **6,** 19159 (2016).
17. Peimyoo, N. *et al.* Nonblinking, Intense Two-Dimensional Light Emitter: Monolayer WS_2 Triangles. *ACS Nano* **7,** 10985–10994 (2013).
18. Kang, K. *et al.* High-mobility three-atom-thick semiconducting films with wafer-scale homogeneity. *Nature* **520,** 656–660 (2015).
19. Stier, A. V., McCreary, K. M., Jonker, B. T., Kono, J. & Crooker, S. A. Exciton diamagnetic shifts and valley Zeeman effects in monolayer WS_2 and MoS_2 to 65 Tesla. *Nat. Commun.* **7,** 10643 (2016).
20. Berghäuser, G. & Malic, E. Analytical approach to excitonic properties of MoS_2. *Phys. Rev. B* **89,** 125309 (2014).
21. Geim, A. K. & Grigorieva, I. V. Van der Waals heterostructures. *Nature* **499,** 419–425 (2013).
22. Fang, H. *et al.* Strong interlayer coupling in van der Waals heterostructures built from single-layer chalcogenides. *Proc. Natl. Acad. Sci.* **111,** 6198–6202 (2014).
23. Ceballos, F., Bellus, M. Z., Chiu, H.-Y. & Zhao, H. Ultrafast Charge Separation and Indirect Exciton Formation in a MoS_2–$MoSe_2$ van der Waals Heterostructure. *ACS Nano* **8,** 12717–12724 (2014).
24. Rivera, P. *et al.* Valley-polarized exciton dynamics in a 2D semiconductor heterostructure. *Science* **351,** 688–691 (2016).
25. Xu, Z.-Q. *et al.* Synthesis and Transfer of Large-Area Monolayer WS_2 Crystals: Moving Toward the Recyclable Use of Sapphire Substrates. *ACS Nano* **9,** 6178–6187 (2015).
26. Su, L., Yu, Y., Cao, L. & Zhang, Y. Effects of substrate type and material-substrate bonding on high-temperature behavior of monolayer WS_2. *Nano Res.* **8,** 1–12 (2015).
27. Elías, A. L. *et al.* Controlled Synthesis and Transfer of Large-Area WS_2 Sheets: From Single Layer to Few Layers. *ACS Nano* **7,** 5235–5242 (2013).
28. Cong, C. *et al.* Synthesis and Optical Properties of Large-Area Single-Crystalline 2D Semiconductor WS_2 Monolayer from Chemical Vapor Deposition. *Adv. Opt. Mater.* **2,** 131–136 (2014).
29. Berkdemir, A. *et al.* Identification of individual and few layers of WS_2 using Raman Spectroscopy. *Sci Rep* **3,** 1755 (2013).
30. Zhang, X. *et al.* Phonon and Raman scattering of two-dimensional transition metal dichalcogenides from monolayer, multilayer to bulk material. *Chem. Soc. Rev.* **44,** 2757–2785 (2015).
31. Li, X. *et al.* Large-Area Synthesis of High-Quality and Uniform Graphene Films on Copper Foils. *Science* **324,** 1312–1314 (2009).
32. Mak, K. F. *et al.* Tightly bound trions in monolayer MoS_2. *Nat Mater* **12,** 207–211 (2013).
33. Lien, D.-H. *et al.* Engineering Light Outcoupling in 2D Materials. *Nano Lett.* **15,** 1356–1361 (2015).
34. Hanbicki, A. T., Currie, M., Kioseoglou, G., Friedman, A. L. & Jonker, B. T. Measurement of high exciton binding energy in the monolayer transition-metal dichalcogenides WS_2 and WSe_2. *Solid State Commun.* **203,** 16–20 (2015).
35. Chakraborty, B. *et al.* Symmetry-dependent phonon renormalization in monolayer MoS_2 transistor. *Phys. Rev. B* **85,** 161403 (2012).
36. Conley, H. J. *et al.* Bandgap Engineering of Strained Monolayer and Bilayer MoS_2. *Nano Lett.* **13,** 3626–3630 (2013).
37. Wang, Y., Cong, C., Qiu, C. & Yu, T. Raman Spectroscopy Study of Lattice Vibration and Crystallographic Orientation of Monolayer MoS_2 under Uniaxial Strain. *Small* **9,** 2857–2861 (2013).
38. Chang, C.-H., Fan, X., Lin, S.-H. & Kuo, J.-L. Orbital analysis of electronic structure and phonon dispersion in MoS_2, $MoSe_2$, WS_2, and WSe_2 monolayers under strain. *Phys. Rev. B* **88,** 195420 (2013).
39. Ghorbani-Asl, M., Borini, S., Kuc, A. & Heine, T. Strain-dependent modulation of conductivity in single-layer transition-metal dichalcogenides. *Phys. Rev. B* **87,** 235434 (2013).
40. Liu, Z. *et al.* Strain and structure heterogeneity in MoS_2 atomic layers grown by chemical vapour deposition. *Nat Commun* **5,** 5246 (2014).
41. Currie, M., Hanbicki, A. T., Kioseoglou, G. & Jonker, B. T. Optical control of charged exciton states in tungsten disulfide. *Appl. Phys. Lett.* **106,** 201907 (2015).
42. Plechinger, G. *et al.* Identification of excitons, trions and biexcitons in single-layer WS_2. *Phys. Status Solidi RRL – Rapid Res. Lett.* **9,** 457–461 (2015).

43. Kim, M. S. *et al.* Biexciton Emission from Edges and Grain Boundaries of Triangular WS_2 Monolayers. *ACS Nano* **10,** 2399–2405 (2016).
44. Zhu, B., Chen, X. & Cui, X. Exciton Binding Energy of Monolayer WS_2. *Sci. Rep.* **5,** 9218 (2015).
45. Nan, H. *et al.* Strong Photoluminescence Enhancement of MoS_2 through Defect Engineering and Oxygen Bonding. *ACS Nano* **8,** 5738–5745 (2014).
46. Tongay, S. *et al.* Broad-Range Modulation of Light Emission in Two-Dimensional Semiconductors by Molecular Physisorption Gating. *Nano Lett.* **13,** 2831–2836 (2013).
47. Bui, V. Q., Pham, T.-T., Le, D. A., Thi, C. M. & Le, H. M. A first-principles investigation of various gas (CO, H_2O, NO, and O_2) absorptions on a WS_2 monolayer: stability and electronic properties. *J. Phys. Condens. Matter* **27,** 305005 (2015).
48. Zhou, C. J., Yang, W. H., Wu, Y. P., Lin, W. & Zhu, H. L. Theoretical study of the interaction of electron donor and acceptor molecules with monolayer WS_2. *J. Phys. Appl. Phys.* **48,** 285303 (2015).
49. Mitioglu, A. A. *et al.* Optical manipulation of the exciton charge state in single-layer tungsten disulfide. *Phys. Rev. B* **88,** 245403 (2013).
50. Balog, R. *et al.* Atomic Hydrogen Adsorbate Structures on Graphene. *J. Am. Chem. Soc.* **131,** 8744–8745 (2009).
51. He, K. T., Wood, J. D., Doidge, G. P., Pop, E. & Lyding, J. W. Scanning Tunneling Microscopy Study and Nanomanipulation of Graphene-Coated Water on Mica. *Nano Lett.* **12,** 2665–2672 (2012).
52. Ishigami, M., Chen, J. H., Cullen, W. G., Fuhrer, M. S. & Williams, E. D. Atomic Structure of Graphene on SiO_2. *Nano Lett.* **7,** 1643–1648 (2007).
53. Haigh, S. J. *et al.* Cross-sectional imaging of individual layers and buried interfaces of graphene-based heterostructures and superlattices. *Nat. Mater.* **11,** 764–767 (2012).
54. Kou, L., Du, A., Chen, C. & Frauenheim, T. Strain engineering of selective chemical adsorption on monolayer MoS_2. *Nanoscale* **6,** 5156–5161 (2014).
55. Keong Koh, E. W., Chiu, C. H., Lim, Y. K., Zhang, Y.-W. & Pan, H. Hydrogen adsorption on and diffusion through MoS_2 monolayer: First-principles study. *Int. J. Hydrog. Energy* **37,** 14323–14328 (2012).
56. Ganji, M. D., Sharifi, N., Ghorbanzadeh, A. & Khosravi, A. Density functional theory calculations of hydrogen molecule adsorption on monolayer molybdenum and tungsten disulfide. *Phys. E Low-Dimens. Syst. Nanostructures* **57,** 28–34 (2014).
57. Svatek, S. A. *et al.* Adsorbate-Induced Curvature and Stiffening of Graphene. *Nano Lett.* **15,** 159–164 (2015).
58. Amft, M., Lebègue, S., Eriksson, O. & Skorodumova, N. V. Adsorption of Cu, Ag, and Au atoms on graphene including van der Waals interactions. *J. Phys. Condens. Matter* **23,** 395001 (2011).
59. Zhan-Yu, W. *et al.* Effects of in-plane stiffness and charge transfer on thermal expansion of monolayer transition metal dichalcogenide. *Chin. Phys. B* **24,** 026501 (2015).
60. Zhang, X., Zhang, X., Wang, A. & Huang, Z. Microstructure and properties of HVOF sprayed Ni-based submicron WS_2/CaF_2 self-lubricating composite coating. *Trans. Nonferrous Met. Soc. China* **19,** 85–92 (2009).

Acknowledgements

Core programs at NRL and the NRL Nanoscience Institute supported this work. This work was supported in part by the Air Force Office of Scientific Research under contract number AOARD 14IOA018-134141. The work at Ohio State was supported by NSF (DMR-1310661). The authors acknowledge use of facilities in the NRL Nanoscience Institute and thank Dean St. Amand and Walter Spratt for technical support. M.I. was supported by the National Science Foundation Grant No. 0955625.

Author Contributions

K.M.M. performed the CVD synthesis of samples. K.M.M. and A.T.H. performed optical characterization. S.S. performed PDMS stamp transfer. G.G.J. performed XPS measurements. M.I., A.N., T.H.B. and R.M.S. acquired TEM images. K.M.M. wrote the manuscript with input from A.T.H, S.S., R.K.K., G.G.J., M.I., A.N., T.H.B., R.M.S. and B.T.J.

Additional Information

Supplementary information accompanies this paper at http://www.nature.com/srep

Competing financial interests: The authors declare no competing financial interests.

How to cite this article: McCreary, K. M. *et al.* The Effect of Preparation Conditions on Raman and Photoluminescence of Monolayer WS_2. *Sci. Rep.* **6**, 35154; doi: 10.1038/srep35154 (2016).